Earth and Planetary Science Letters 384 (2013) 132–143

Contents lists available at ScienceDirect

Earth and Planetary Science Letters

www.elsevier.com/locate/epsl

Contrasting behavior of oxygen and iron isotopes in banded iron formations revealed by *in situ* isotopic analysis

Weiqiang Li [a,b,*], Jason M. Huberty [a,b], Brian L. Beard [a,b], Noriko T. Kita [a,b], John W. Valley [a,b], Clark M. Johnson [a,b]

[a] University of Wisconsin–Madison, Department of Geoscience, 1215 West Dayton Street, Madison, WI 53706, United States
[b] NASA Astrobiology Institute, United States

ARTICLE INFO

Article history:
Received 18 June 2013
Received in revised form 8 October 2013
Accepted 8 October 2013
Available online 1 November 2013
Editor: T.M. Harrison

Keywords:
Dales Gorge member BIF
Fe isotopes
O isotopes
SIMS
femtosecond laser ablation
MCICP-MS

ABSTRACT

In situ O and Fe isotope measurements of magnetite and hematite in banded iron formations (BIFs) from the 2.5 Ga Dales Gorge member of the Brockman Iron Formation, Hamersley Group, Western Australia, document distinct fine-scale isotopic zonation. For hematite, $\delta^{18}O$ values (VSMOW) range from −7.1 to −0.6‰, and $\delta^{56}Fe$ values range from −0.50 to +1.53‰. Magnetite has a $\delta^{18}O$ range of −5.6 to +7.0‰ and a $\delta^{56}Fe$ range of −0.76 to +1.33‰. Notably, magnetite shows significant O isotope variability at a <100 μm scale in individual magnetite grains or layers, where up to 6‰ difference in $\delta^{18}O$ values exists between low-Si core and Si-rich overgrowth. Iron isotope compositions are homogeneous to ±0.2‰ in $\delta^{56}Fe$ values within individual grains or layers. Hematite is always isotopically heavier than co-existing magnetite by 0.1–0.4‰ in $\delta^{56}Fe$ within individual samples, and there is a large variation (>2‰) in $\delta^{56}Fe$ values between BIF samples at the > m-scale (e.g., between meso- or macro-bands of the Dales Gorge Member). *In situ* isotopic results highlight the distinct behavior of O and Fe isotopes during interaction with post-deposition diagenetic or metamorphic fluids. The large variations in $\delta^{18}O$ values of iron oxides likely reflect exchange with fluids during post-depositional events at temperatures up to ca. 280 °C, and the lower $\delta^{18}O$ values of Fe oxides are interpreted to reflect less isotopic modification and lower temperatures. $\delta^{18}O$ variations support a model where initial $Fe(OH)_3$ precipitates that formed in the photic zone were converted to hematite during very early diagenesis, followed by production of magnetite over a range of temperatures during later diagenesis/metamorphism. In contrast, magnetite and hematite seem to have preserved the initial $\delta^{56}Fe$ values of early $Fe(OH)_3$ precipitates, despite significant changes in O isotope compositions in magnetite. The consistency in apparent Fe isotope fractionation between co-existing hematite and magnetite suggests that they share a common precursor, where magnetite was formed in soft sediment through *in situ* reduction by microbial processes, and possibly including reaction with aqueous Fe(II). Combined *in situ* Fe–O isotope analyses allow distinctions to be made between near-primary and post-depositional signatures in BIFs, which bears on the use of BIFs as paleo-environmental proxies and recorders of microbial processes.

1. Introduction

Banded iron formations (BIFs) are marine chemical precipitates that contain >15 wt.% Fe that consist of iron- and silica-rich layers (James, 1954), and widely occur in Archean and Paleoproterozoic terranes (e.g., Klein, 2005; Trendall and Morris, 1983). BIFs record periods of Earth's geologic history when abundant, hydrothermally-sourced aqueous Fe(II) was removed from Archean and Proterozoic oceans through oxidation and precipitation as Fe(III) oxides and hydroxides (Holland, 1984). As such, BIFs have figured prominently in discussions on the paleo-environmental conditions of the early Earth, including the redox structure of Precambrian oceans, and recent reviews may be found in Klein (2005) and Bekker et al. (2010). The use of BIFs as a proxy for the ancient oceans may be complicated by the protracted diagenetic and metamorphic histories of BIFs. Fundamental to this issue is determining if BIF minerals formed in equilibrium with the oceans (Johnson et al., in press).

Stable isotope compositions of O in BIF minerals, including quartz, magnetite, and siderite, as well as C isotope compositions of Fe carbonates, have been used to infer paleo-environmental conditions, as well as post-depositional processes such as diagenesis and metamorphism that may later occur in BIFs (Baur et al., 1985; Becker and Clayton, 1972, 1976; Kaufman, 1996; Kaufman et al., 1990; Perry et al., 1973; Winter and Knauth, 1992). Specifically, O isotope compositions of BIFs have been used to infer paleo-temperatures, but it also has been recognized that O isotopes

* Corresponding author.
E-mail addresses: wli@geology.wisc.edu, liweiq@gmail.com (W. Li).

0012-821X/$ – see front matter
http://dx.doi.org/10.1016/j.epsl.2013.10.014

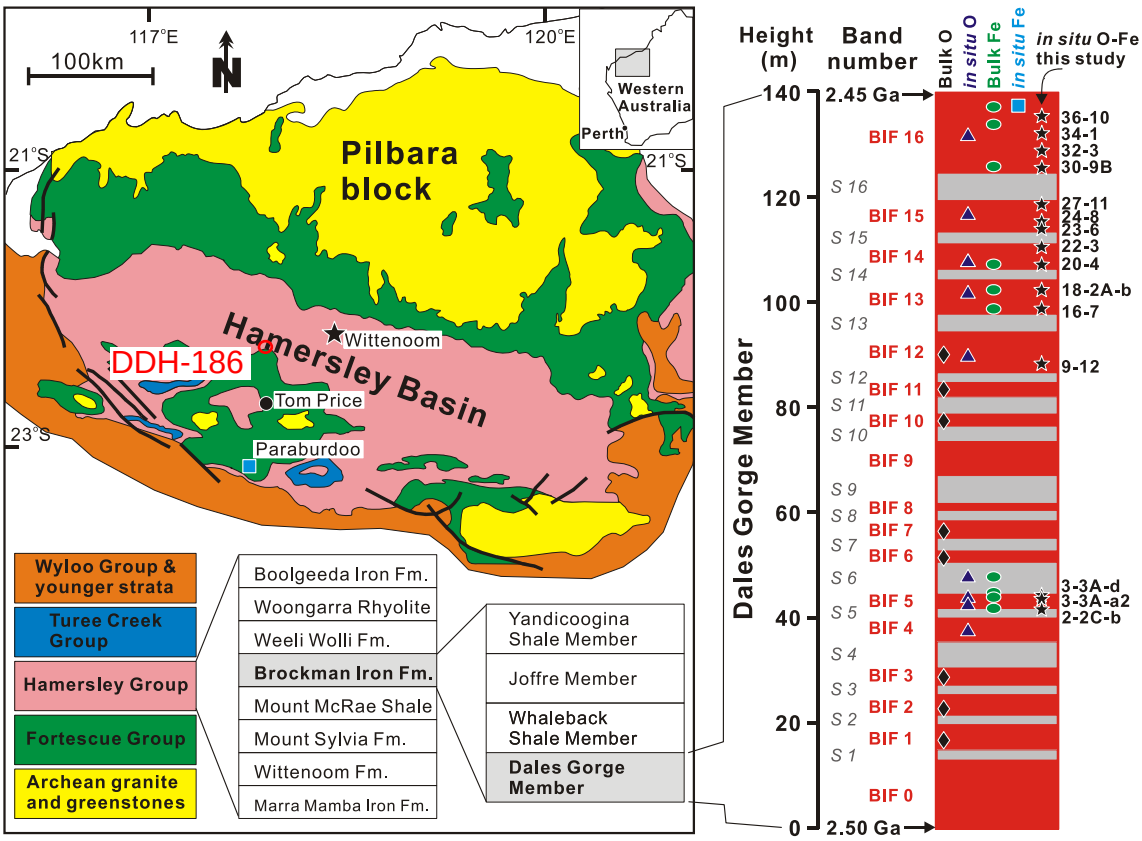

Fig. 1. Geological background of the Dales Gorge Member BIF of Hamersley Basin, Western Australia. Figure is modified after Trendall et al. (2004) and Johnson et al. (2008a). The 2.50–2.45 Ga age for the Dales Gorge Member BIF was based on zircon U–Pb geochronology constraints (Trendall et al., 2004). The Drill core DDH-47(A) was drilled ~15 km south of Wittenoom (filled star). Prior to the present *in situ* Fe and O isotope study, samples from Drill core DDH-47(A) have been studied by analyzing O isotope composition of bulk mineral separates (black diamond; Becker and Clayton, 1976), O isotope composition of quartz using SIMS (blue triangle; Huberty et al., 2010a; Heck et al., 2011), Fe isotope composition of bulk mineral separates using solution-nebulization MC-ICP-MS (green oval; Johnson et al., 2008a). Another *in situ* Fe isotope study on the Dales Gorge Member BIF has been reported by Steinhoefel et al. (2010), and they investigated a sample from BIF band 16 from drill core DDH-44 at Paraburdoo (light blue square). Samples of Drill core DDH-47(A) that were analyzed in this study are marked with black stars. (For interpretation of the references to color in this figure, the reader is referred to the web version of this article.)

may provide information on fluid–mineral interactions and temperatures of equilibration or isotopic exchange (Gregory and Criss, 1986; Hyslop et al., 2008; Valley, 2001). Carbon isotope compositions have been used to infer the relative contributions of biologic and abiologic C sources. More recently, studies using Fe isotope geochemistry have investigated abiologic versus biologic pathways for BIF mineral formation (e.g., Craddock and Dauphas, 2011; Heimann et al., 2010; Johnson et al., 2003, 2008a, 2008b; Planavsky et al., 2012; Rouxel et al., 2005; Steinhoefel et al., 2010). In addition, Si isotope studies of BIFs have focused on distinguishing weathering and hydrothermal sources of silica (Heck et al., 2011; Steinhoefel et al., 2010).

The ubiquitous fine-scale variations in mineralogical and petrographic relations of BIFs, which may record primary depositional features or soft-sediment diagenesis (e.g., Ewers and Morris, 1981; Trendall and Morris, 1983), indicate that *in situ* analysis approaches are more likely to provide a full understanding of BIF genesis than bulk analysis methods. Recent developments in Secondary Ion Mass Spectrometry (SIMS) have enabled relatively high precision *in situ* O isotope ratio measurements of Fe oxides (Huberty et al., 2010b). *In situ* Fe isotope analyses of Fe oxides using femtosecond Laser Ablation (fs-LA) multi-collector ICP-MS have been reported, demonstrating great promise for widespread application of *in situ* isotopic analysis of Fe-bearing minerals (Czaja et al., 2013; Horn et al., 2006; Steinhoefel et al., 2009, 2010; Yoshiya et al., 2012). SIMS analyses of Fe isotopes in magnetite have also been reported (Marin-Carbonne et al., 2011; Whitehouse and Fedo, 2007), although Kita et al. (2011) show that an orientation effect exists for isotopic analysis of magnetite for both O and Fe isotopes, which may create spurious apparent variability. In this study, we present results of the first combined *in situ* O and Fe isotope investigation of BIF samples from the most voluminous interval of BIF deposition in Earth history, specifically, the 2.5 Ga Dales Gorge member of the Brockman Iron Formation, Hamersley Group, Western Australia. These new results demonstrate that O and Fe isotopes may record distinct processes during BIF mineral formation, early diagenesis, fluid–mineral interaction, and metamorphism. Combined, these two isotope systems, when measured on a mineral scale, provide new insights into the origin of BIFs and their use as tracers of paleo-environmental conditions, ancient ocean proxies, and the role of microbial processes.

2. Geological background and samples

The Hamersley Basin in Western Australia contains the world's most extensive Superior-type BIFs (Trendall and Blockley, 1970). The Paleoproterozoic Hamersley Group includes three major BIF units, which are, from older to younger, the Marra Mamba, Brockman, and Boolgeeda iron formations. The Dales Gorge member of the lowermost part of the Brockman Iron Formation (IF) is the subject of this study (Fig. 1). The depositional age of the Dales Gorge member lies between 2.50 Ga and 2.45 Ga (Trendall et al., 2004). The Dales Gorge member is approximately 160 m thick, consisting of 17 iron-rich, m-scale macro-bands and 16 shale macro-bands, named BIF0–BIF16 and S1–S16, respectively (Fig. 1). The

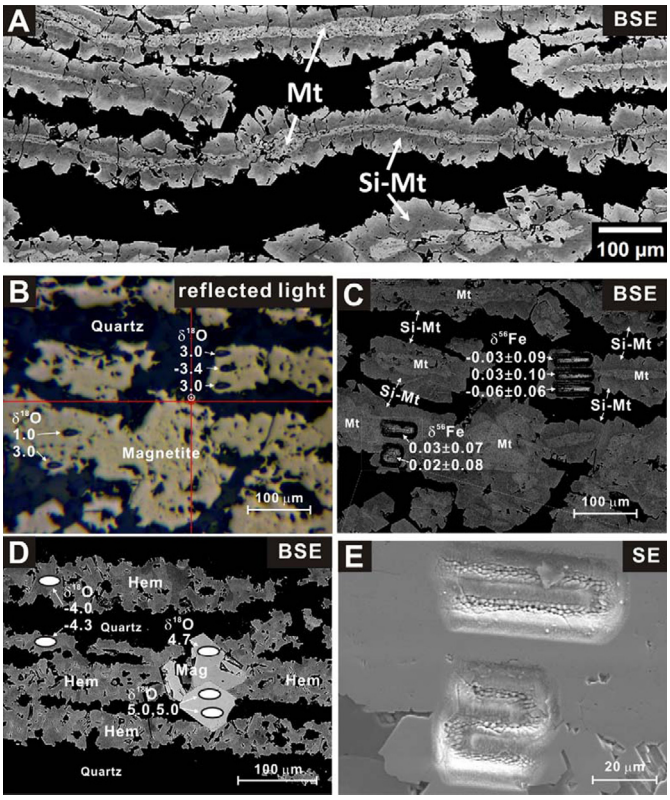

Fig. 2. Representative mineral textures and pits of *in situ* isotope analyses. A: BSE image of sample 3-3 showing typical low-Si magnetite (Mt) and silician magnetite (Si–Mt) over growths (modified from Huberty et al., 2012); condition of the BSE detection was optimized to show the contrast between the darker silician magnetite overgrowths and the brighter low-Si magnetite cores. B: Photomicrograph of representative magnetite layers (sample 22-3) under reflected light, screen-captured from the camera of fs-laser ablation system. Black ovals marked by white arrows are pits after SIMS oxygen isotope analyses, and numbers next them are in situ $\delta^{18}O$ values, same in Fig. 2D. C: BSE image of magnetite layer of sample 22-3, field of view is the same as Fig. 2B. BSE image was taken after fs-laser ablation analyses for Fe isotopes, which were made to superimpose the SIMS pits. Both SIMS and fs-laser ablation analyses were made based on BSE images so only a single type of magnetite was analyzed. The laser ablation pits show black edges and bright centers in BSE images and number next to them are measured $\delta^{56}Fe$ values with internal 2 SE errors. D: Photomicrograph of representative hematite layers with euhedral magnetite with recrystallization texture (sample 16-7). E: Secondary electron image of representative fs-laser ablation pits made on magnetite; this is an enlargement of the lower-left part of Fig. 2C.

m-scale iron-rich macro-bands are composed of cm-scale iron-rich mesobands, which contain numerous sub-mm micro-bands (Trendall and Blockley, 1968), and these bands show continuity over >100 km across the Hamersley Basin (Ewers and Morris, 1981). Metamorphic grade is estimated at lower greenschist facies (Ewers and Morris, 1981).

The BIF samples analyzed in this study come from diamond drill core DDH-47A that was drilled ~15 km south of Wittenoom, Western Australia (Fig. 1). DDH-47A is the type section core for the Dales Gorge member that has been described in detail (Trendall and Blockley, 1968). This drill core has been studied in previous C, O, and Fe isotope investigations using mg-sized, bulk-sampling techniques (Becker and Clayton, 1972, 1976; Johnson et al., 2008a). The samples studied here via *in situ* analysis for O and Fe isotopes are from the same sample suite used by Johnson et al. (2008a), Heck et al. (2011), and Huberty et al. (2012).

Magnetite and hematite are the typical Fe-bearing minerals in the DDH-47A drill core samples (Fig. 2). Based on reflected-light microscopy and detailed BSE imaging, Huberty et al. (2012) noted that magnetite in the BIF samples can be divided into three groups. The first group occurs as discrete, large (typically >50 μm), euhedral, apparently-homogeneous grains that are interpreted as a recrystallization texture, and we refer to this as *euhedral magnetite*. Euhedral magnetite commonly occurs in samples that contain predominant hematite and minor magnetite (e.g., Fig. 2D). The other two groups of magnetite are termed *silician magnetite* and *low-Si magnetite*, where the former contains 1–3 wt.% SiO_2, and the latter contains <1 wt.% SiO_2. The silician and low-Si magnetite have distinctive contrast in BSE images, and silician magnetite commonly forms overgrowths to low-Si magnetite domains (e.g., Figs. 2A, 2C; Huberty et al., 2012). Importantly, Huberty et al. (2012) demonstrated that Si substitution occurred in the magnetite crystal lattice, and did not reflect fine-scale mineral intergrowths. Silician magnetite and low-Si magnetite commonly occur in BIF samples that contain extensive magnetite layers but no hematite. In terms of paragenetic sequence, low-Si magnetite is interpreted to be the earliest of the three magnetite groups (Huberty et al., 2012).

3. Analytical methods

3.1. Notation

Oxygen isotope data are reported as $^{18}O/^{16}O$ ratios in standard delta (δ) notation, in units of per mil (‰):

$$\delta^{18}O = \left[\left(^{18}O/^{16}O\right)_{sample}/\left(^{18}O/^{16}O\right)_{standard} - 1\right] \times 1000 \quad (1)$$

where the standard is VSMOW. Iron isotope data are reported as $^{56}Fe/^{54}Fe$ and $^{57}Fe/^{54}Fe$ ratios in standard δ notation, in units of per mil (‰):

$$\delta^{5x}Fe = \left[\left(^{5x}Fe/^{54}Fe\right)_{sample}/\left(^{5x}Fe/^{54}Fe\right)_{standard} - 1\right] \times 1000 \quad (2)$$

where $x = 6$ or 7, and the average of igneous rocks is the standard reference reservoir (Beard et al., 2003). Relative to the average of igneous rocks, the international Fe isotope standard IRMM-014 has a $\delta^{56}Fe$ value of −0.09‰ on this scale (Beard et al., 2003). Isotopic fractionation between two phases A and B is expressed as:

$$\Delta^{18}O_{A-B} = \delta^{18}O_A - \delta^{18}O_B \quad (3)$$

for O isotopes, and

$$\Delta^{56}Fe_{A-B} = \delta^{56}Fe_A - \delta^{56}Fe_B \quad (4)$$

for Fe isotopes, following standard conventions.

3.2. Sample preparation

Millimeter- to centimeter-sized rock chips were cut for fifteen samples from six BIF macro-bands (BIF 5, 12–16) from the DDH-47A drill core, using a thin diamond saw blade, and then embedded near the center of 1-inch (2.5 cm diameter) round epoxy plugs, where grains of a well-characterized quartz standard (UWQ-1, Kelly et al., 2007) were embedded as a reference standard for SIMS oxygen isotope analysis. The plugs were polished following a protocol described by Heck et al. (2011) to produce a smooth, flat sample surface with relief less than a few μm, which is critical for high-accuracy, high-precision isotope ratio analysis by SIMS (Kita et al., 2009, 2011). The same plugs were subsequently used for Fe isotope analysis.

3.3. Scanning electron microscopy

Samples were imaged using a Hitachi S-3400N scanning electron microscope using secondary electron imaging (SEM) and backscattered electron (BSE) mode, both before and after SIMS and fs-LA isotopic analyses, to ensure that analysis did not penetrate additional minerals, inclusions, or cracks. Spot analyses using

Energy-Dispersive X-ray Spectroscopy (EDS) were performed using an accelerating voltage of 15 kV, a working distance of 9 mm, and Thermo Scientific NORAN System SIX software.

3.4. Oxygen isotope analysis

In situ O isotope analysis was performed via SIMS using a CAMECA IMS-1280 Ion Microprobe at the WiscSIMS Laboratory, University of Wisconsin-Madison. All analyses were made based on detailed SEM and BSE images to avoid defects and contamination from other phases, and analysis spots were located within 5 mm from the center of the plug to keep the spatial instrumental mass bias ("XY effect", Kita et al., 2009) below the external reproducibility. A well-characterized UWQ-1 quartz standard was used as the bracketing standard for instrumental bias correction, following the bracketing methods described in detail by Huberty et al. (2010b). The instrumental bias correction factors for hematite and magnetite were calibrated by δ^{18}O measurements of homogeneous Fe oxide standards relative to that of UWQ-1 quartz standard grains mounted in the same mount, which were then applied to the unknown samples.

Analysis of O isotope ratios in magnetite and hematite was performed using a special "low-kV" technique that is designed to minimize orientation effects in Fe-oxides, which have been reported from SIMS analysis of O (and Fe) isotopes in hematite and magnetite (Huberty et al., 2010b; Kita et al., 2011) using conventional SIMS settings. The crystal orientation effects can be significantly reduced by decreasing the total impact energy of the incident Cs^+ beam, and by increasing the incident Cs^+ beam angle to the sample surface (Huberty et al., 2010b; Kita et al., 2011). The "low-kV" technique produces pits on samples with a dimension of 5×15 μm (Fig. 2). Based on δ^{18}O measurements of homogeneous standards over multiple sessions, the external precision (reproducibility) of this method is ±0.8‰ (2 SD) for magnetite, and ±1.0‰ (2 SD) for hematite (Huberty et al., 2010b).

3.5. Iron isotope analysis

In situ Fe isotope analysis was performed using a femtosecond Laser Ablation (fs-LA) MC-ICP-MS system at the Radiogenic Isotope Laboratory, University of Wisconsin-Madison. The system consists of a femtosecond source laser that produces an output 266 nm beam that has a pulse width of ~ 130 fs, a Photon-Machines beam-delivery system and a Photon-Machines HelEX ablation cell, and a Micromass *IsoProbe* MC-ICP-MS. Laser ablation analysis was made in raster mode, with the stage moving at a speed of 1 μm/s, and typically in a rectangle area of 30×50 μm (Fig. 2). For samples that had elongated shapes, analysis consisted of non-rectangular rasters at 1 μm/s. Ablation rasters were often placed directly on top of SIMS pits, as LA is relatively immune to sample topography. Details of the operating conditions of the fs-LA system are listed in Appendix 1 (Table A1-1), and can be found in Czaja et al. (2013).

A standard-sample-standard bracketing method was used for mass bias and instrument drift correction. A magnetite in-house standard and a hematite in-house standard were used as the matrix-matching standards for fs-LA Fe isotope analysis of magnetite and hematite samples, respectively. Stable isotope analysis by fs-LA is not affected by crystal orientation. Conventional MC-ICP-MS analyses confirmed that the two standards are isotopically homogeneous (Appendix 1). Using matrix-matching standards and the HelEX cell, total Fe signal intensities of standards and samples were typically matched within 5%, except for analyses in which quartz was accidentally ablated. The internal precision of each Fe isotope analysis was typically better than 0.12‰ (2 SE) in both δ^{56}Fe and δ^{57}Fe values. Measured δ^{56}Fe and δ^{57}Fe values followed a mass-dependent relation (Appendix 1, Fig. A1-1). External precision (reproducibility) of the fs-LA analysis was better than ±0.2‰ (2SD) in δ^{56}Fe, based on repeat analyses of the same magnetite and hematite standards within an analytical session and over multiple sessions. Accuracy of fs-LA MC-ICP-MS Fe isotope analysis lies within the external reproducibility (<0.2‰ in δ^{56}Fe, 2 SD; Appendix 1).

4. Results

Oxygen isotope ratios of magnetite and hematite were measured by SIMS, followed by fs-LA Fe isotope measurements on top of the existing SIMS pits. Fig. 2 shows O and Fe isotope results that are typical of those found for the different groups of magnetite, particularly the relations between silician and low-Si magnetite. A summary of the O and Fe isotope data is plotted in Fig. 3 relative to stratigraphic height of the Dales Gorge member. Detailed results for individual O and Fe isotope analyses are tabulated in Appendix 2. Photomicrographs showing the isotope results with textural details of the *in situ* analyses are provided in Appendix 3.

4.1. Oxygen isotope results

In situ O isotope analyses ($n = 175$) document significant isotopic variability in iron oxide minerals of the Dales Gorge member BIF. The 15 samples analyzed from six BIF macro-bands show a typical 10‰ variation in δ^{18}O values in each sample (Fig. 3), which greatly exceeds the 0.8–1.0‰ external precision (2SD) for δ^{18}O measurements using the "low-kV" procedure. The greatest *O* isotope variation (up to ~ 16‰) in iron oxides was found in samples from BIF band 5, where the largest number of analyses was made. Although oxygen isotope variations in BIF band 12 appear to be small, this observation may not be representative due to the small number of SIMS analyses ($n = 4$) made on this sample. The O isotope variability in iron oxide minerals contrasts with the narrow δ^{18}O range (21–22‰) for quartz from the Dales Gorge member BIF (Heck et al., 2011; Huberty et al., 2010a).

The first-order control on O isotope variations in the BIF samples is mineralogy. As shown in Figs. 3 and 4, hematite always has negative δ^{18}O values, ranging from −8.8 to −0.6‰, whereas euhedral magnetite grains always have positive δ^{18}O values, ranging from +2.7 to +7.0‰. Silician magnetite also has positive δ^{18}O values that tightly cluster between +2.0 and +4.5‰, with a few exceptions, and low-Si magnetite shows a wide range of δ^{18}O values from −5.6 to +3.8‰, generally lying between the δ^{18}O ranges of hematite and silician magnetite (Figs. 3 and 4; Appendix 2). In some cases, significant gradients in δ^{18}O between silician magnetite and low-Si magnetite can be distinguished from SIMS pits 5–10 μm apart (Appendix 3, p11), the limit of the spatial resolution of these data.

The large range in δ^{18}O values for magnetite measured here by SIMS, from ~−6 to +7‰, is consistent with, but significantly more variable than, the δ^{18}O range of 0 to 5‰ that was measured from mineral concentrates from the Dales Gorge member BIF by Becker and Clayton (1976). Similarly, the range in δ^{18}O values for hematite measured here by SIMS, from ~−9 to −1‰, significantly expands the δ^{18}O range measured for hematite mineral separates by Becker and Clayton (1976), which was relatively constant at −2‰. These contrasts demonstrate the importance of *in situ* isotopic analysis in determining the true range of isotopic variation, and the relations in Fig. 2 indicate that bulk mineral separates likely include multiple generations of minerals that, individually, may have distinct isotopic compositions.

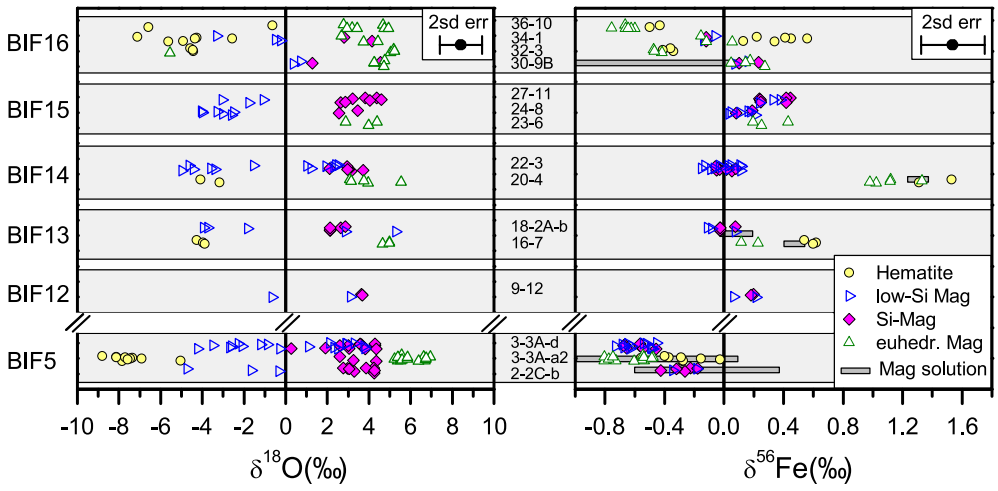

Fig. 3. Plot of O and Fe isotope data along the drill core DDH-47A. The *y*-coordinates for the data points show the relative position of the samples along the drill core, and they are NOT proportional to the actual depth along the drill core. Data are separated into four groups, which are hematite, low-Si magnetite, silician magnetite, and euhedral magnetite. For definition of the four groups, see Section 4.1. Dark bands in the right diagram show δ^{56}Fe range for bulk magnetite mineral separates measured by solution nebulization MCICP-MS by Johnson et al. (2008a). Note that the Johnson et al. (2008a) sampled multiple layers from drill cores of over several centimeters for each sample, whereas in this study, each sample is a sub-centimeter sized chip of the drill core.

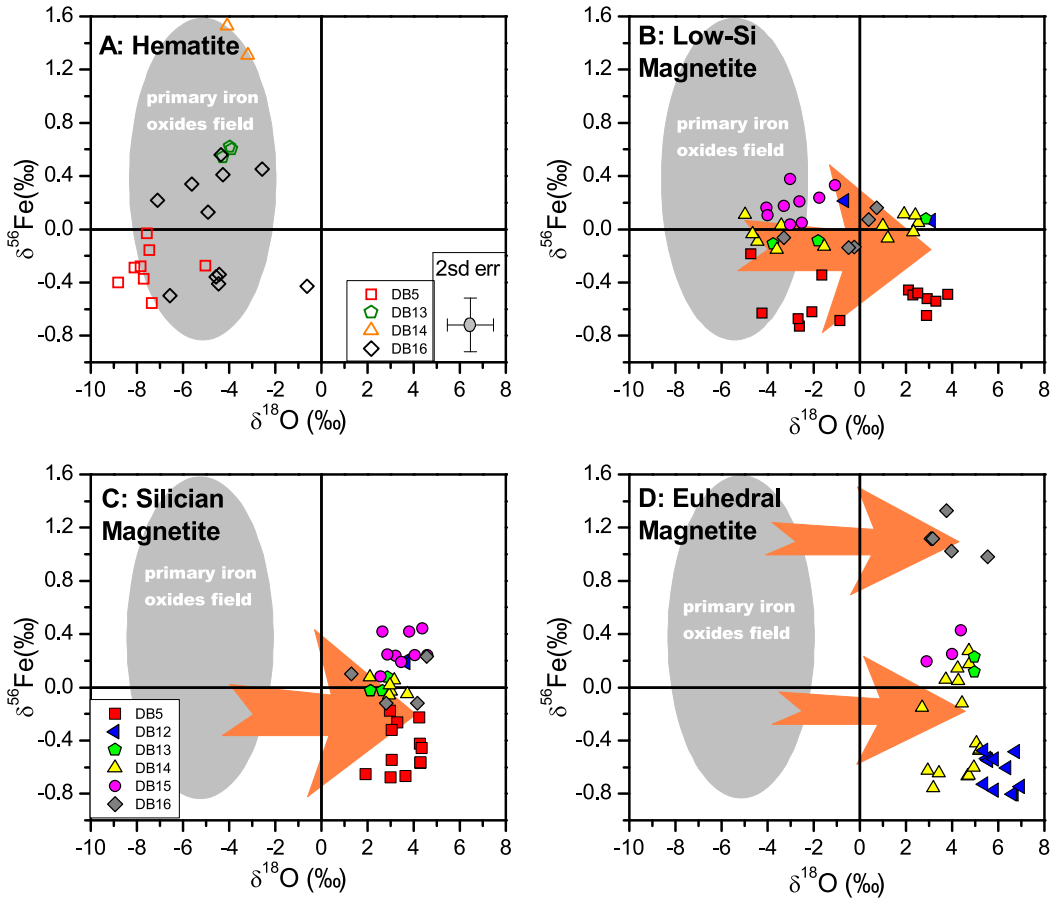

Fig. 4. Plot of O–Fe isotope data for hematite (A), low-Si magnetite (B), silician magnetite (C), and euhedral magnetite (D). Samples are grouped by band number. The shaded oval area denotes the isotopic compositions of the earliest formed hematite and magnetite. Post-depositional processes produced elevated δ^{18}O values for magnetite, which is illustrated by the large brown arrows, but little change in Fe isotope compositions. See text for detailed discussion.

4.2. Fe isotope results

Overall, fs-LA analyses document a variation of 2.3‰ in δ^{56}Fe values in the BIF samples (Figs. 3 and 4; Appendix 2). Despite the large Fe isotope variation between samples along the drill core, the range in δ^{56}Fe values for a specific phase (i.e., silician magnetite, low-Si magnetite, hematite) in an individual sample is small, generally within the ±0.2‰ 2SD external precision for fs-LA analysis (Figs. 3 and 4). Importantly, the large O isotope variability among different magnetite groups in the same sample is not observed for Fe isotopes. For example, the δ^{56}Fe values of silician magnetite and low-Si magnetite overlap in individual samples (Fig. 3). These re-

lations are illustrated in Fig. 2, where, for example, although there is a 4–6‰ difference in $\delta^{18}O$ values between low-Si magnetite and silician magnetite within a 30 μm distance, $\delta^{56}Fe$ values of the two magnetite phases are identical within error. Comparison of $\delta^{56}Fe$ values between hematite and magnetite that co-exist in the same sample suggests that the $\delta^{56}Fe$ values of hematite are systematically greater by a small, but significant amount (Fig. 3); this observation is consistent with previous *in situ* studies of BIFs by Steinhoefel et al. (2010).

The largest range in Fe isotope variation is defined across BIF bands and samples that are separated by cm- and m-distances. The lowest $\delta^{56}Fe$ values were found in samples from BIF band 5 and band 16, where $\delta^{56}Fe$ values of magnetite are as low as −0.8‰. The highest $\delta^{56}Fe$ values are in hematite from BIF band 14, which has a $\delta^{56}Fe$ value of +1.5‰ (Figs. 3 and 4; Appendix 2). It is important to note that in several cases, samples from the same BIF macro-band, but taken from different vertical depths along the drill core, have distinct Fe isotope compositions. For example, there is a ∼1‰ difference in $\delta^{56}Fe$ values between the two BIF band 14 samples 20-4 and 22-3 that are ∼2 m apart in drill core, and the four samples from BIF band 16 show alternating positive and negative $\delta^{56}Fe$ values along ∼11 m of drill core (Figs. 1 and 3; appendix of Huberty et al., 2012).

Some of the BIF samples analyzed here using *in situ* methods have been previously analyzed via conventional (bulk) analysis of mg-size samples (Johnson et al., 2008a), and the $\delta^{56}Fe$ values determined by fs-LA show a good agreement with the data measured by conventional methods (Fig. 3). It should be noted that Johnson et al. (2008a) sampled multiple layers in drill cores over several centimeters, which encompassed a larger selection of samples than this study that analyzed sub-centimeter drill core chips (Fig. 3); this observation confirms that Fe isotope variability is greater over cm- and m-distances in the Dales Gorge BIF, rather than on the micron scale.

5. Discussion

Combined *in situ* analyses reveal different patterns of isotopic variability of O and Fe in magnetite and hematite, which implies decoupled behavior of the two elements in BIFs. Because BIF genesis involves a series of events including precipitation, diagenesis, and burial metamorphism, the distinct response of O and Fe isotopes to these processes are discussed below.

5.1. Metamorphism, diffusion, and preservation of O and Fe isotope compositions

The Dales Gorge member BIF of this study near Wittenoom has experienced lower greenschist facies metamorphism at 200–300 °C for up to 70 m.y. duration (Rasmussen et al., 2005), and thus the influence of diffusion on the isotopic compositions of minerals by protracted metamorphism must be assessed. Following the approaches of Watson et al. (2009) and Williford et al. (2011), we calculated the width of the interdiffusion zone for O and Fe between two isotopically different domains of a Fe-oxide mineral (i.e., magnetite or hematite) at a constant metamorphic temperature, assuming one-dimensional diffusion perpendicular to the isotopic boundary (Crank, 1975). As a boundary condition, we assumed that the initial isotopic gradient was a step function. The interdiffusion zone is defined as the distance interval that encompasses 90% of the initial isotopic difference (Watson et al., 2009). We used diffusion coefficients for O in magnetite (Giletti and Hess, 1988), Fe in magnetite and hematite (Hallstrom et al., 2011), and assumed O has the same diffusion coefficient as Fe in hematite based on limited available experimental data (Amami et al., 1999; Chang and Wagner, 1972; Kingery et al., 1960). These results indicate that the maximum widths of interdiffusion zones are ca. 5 μm for O in magnetite, >8000 μm for Fe in magnetite, and <0.01 μm for Fe and O in hematite, assuming metamorphism to 300 °C for a duration of 70 m.y. Although there is some uncertainty in extrapolation of the diffusion coefficients to relatively low temperature as compared to experimental conditions (Giletti and Hess, 1988; Hallstrom et al., 2011), the large difference in calculated interdiffusion zone widths suggests that O and Fe isotope zonation in magnetite and hematite should respond quite differently to metamorphism.

The very small calculated interdiffusion zone width (<0.01 μm) of Fe and O for hematite implies that Fe and O isotope ratios of hematite should not have been significantly modified by metamorphism in the Hamersley Basin; therefore, an intact, μm-sized crystal of hematite in the Hamersley BIF likely preserves its Fe and O isotope compositions after crystallization. The millimeter level of interdiffusion zone width of Fe in magnetite suggests that any initial Fe isotope zonation within a typical magnetite grain (<100 μm) in the BIFs could have been erased by metamorphism, although isotopic differences of Fe between individual magnetite grains or bands that are separated by intervening quartz might be preserved. In contrast, the μm-scale interdiffusion zone width for O in magnetite suggests that O isotope zonation over fine scales, ∼10 μm distances, are likely to be preserved. In summary, calculations for O and Fe diffusion in magnetite are consistent with the *in situ* isotope analyses, where apparent Fe isotope homogeneity in magnetite grains and adjacent bands contrasts with the remarkable O isotope zonation that exists between low-Si magnetite cores and silician magnetite overgrowths (e.g., Fig. 2A, B, Appendix 3, p11, p13).

5.2. Oxygen isotope constraints on iron oxide formation

The $\delta^{18}O$ values of iron oxides in the Dales Gorge BIF reflect the combined effects of initial O isotope compositions of the early iron hydroxide precipitates and subsequent interaction with diagenetic and/or metamorphic fluids. Because quartz in the Dales Gorge BIF has high $\delta^{18}O$ values (>20‰; e.g., Becker and Clayton, 1976), and the magnitude of O isotope fractionation between quartz and magnetite decreases as temperature increases (e.g., Clayton and Kieffer, 1991; Zheng, 1991), isotopic exchange between the two minerals (and fluids) at elevated temperatures during post-depositional processes would have increased $\delta^{18}O$ values of magnetite (e.g., Becker and Clayton, 1976). The highest $\delta^{18}O$ values are measured from the euhedral magnetite (Figs. 3 and 4) that shows clear recrystallization textures, indicating formation at relatively high temperature. Silician magnetite overgrowths have higher $\delta^{18}O$ values than the low-Si magnetite cores (e.g., Fig. 2; Appendix 3), indicating that silician magnetite formed later, possibly during burial metamorphism when the temperature had increased significantly (Fig. 4). This is consistent with petrographic relations which indicate that the low-Si magnetite is the earliest magnetite generation (Huberty et al., 2012). Low-Si magnetite shows a large variation in $\delta^{18}O$ values that reflects formation over a wide range of temperature, or different degrees of isotopic exchange during metamorphism (Fig. 4), and magnetite that has the lowest $\delta^{18}O$ values represents the most pristine, least exchanged magnetite.

Because hematite likely preserved the O isotope composition after crystallization due to the very small interdiffusion zone width (Section 5.1), the low $\delta^{18}O$ values for hematite suggest that the lowest $\delta^{18}O$ values of low-Si magnetite (∼−6‰) may be closest to the O isotope composition expected for very early, low-temperature magnetite. Given that currently available experimental studies report limited (0 ± 3‰) hematite–water $^{18}O/^{16}O$ fractionations at <150 °C (Bao and Koch, 1999; Yapp, 1990), we postulate

a similar $\delta^{18}O$ value range (−8 to −4‰) for the fluid that was in equilibrium with early formed hydrous ferric hydroxide [$Fe(OH)_3$], the precursor of hematite and magnetite (e.g., Klein, 2005). This range overlaps with that suggested by Heimann et al. (2010), who modeled a $\delta^{18}O$ range of −2 to −5‰ for fluid during BIF carbonate precipitation, based on studies of BIFs from South Africa that are coeval with the Dales Gorge member BIF.

Both *in situ* SIMS analyses (Heck et al., 2011; Huberty et al., 2010a) and bulk analyses of mineral concentrates (Becker and Clayton, 1976) show that most quartz throughout the stratigraphic column of the Dales Gorge member has a narrow $\delta^{18}O$ range of 21–22‰, despite large variations in band-type and quartz/iron-oxide ratios at scales of sub-millimeter to meters. The limited range of O isotope compositions in quartz is best explained by recrystallization and exchange with a late-stage, pervasive fluid. Given this, the quartz–magnetite oxygen isotope geothermometer can only be applied to the specific generation of magnetite that was formed during this hydrothermal activity that homogenized and reset the O isotopes in quartz. Calculated temperatures, therefore, are the upper limit for the temperature of fluid–rock interaction. Combining the results of Becker and Clayton (1976) and Heck et al. (2011), we set a $\delta^{18}O$ value of 21.5‰ for quartz, and calculated the apparent temperatures for euhedral magnetite and silician magnetite using the $T - \Delta^{18}O_{qz\text{-}mag}$ functions of Clayton and Kieffer (1991) and Zheng (1991). The ranges of calculated apparent temperatures for euhedral magnetite–quartz pairs are 270–350 °C using the Clayton and Kieffer (1991) function and 200–280 °C using the Zheng (1991) function, respectively. The ranges of calculated apparent temperatures for silician magnetite–quartz pairs are 270–330 °C using the Clayton and Kieffer (1991) function and 170–230 °C using the Zheng (1991) function, respectively. These results are consistent with previous proposals of hydrothermal alteration and/or metamorphism up to ~300 °C based on studies of Becker and Clayton (1976) and Rasmussen et al. (2005).

5.3. Iron isotope constraints on iron oxide formation

The most common mechanism proposed for the accumulation of the Fe-rich components in BIFs is oxidation of hydrothermally sourced $Fe(II)_{aq}$ (e.g., Klein, 2005), which should have had a $\delta^{56}Fe$ value of around 0‰, or slightly negative (e.g., Johnson et al., 2008b). We first consider the range of Fe isotope fractionations that could be produced by $Fe(OH)_3$ precipitation in the shallow ocean (photic zone). Under equilibrium conditions, the Fe isotope fractionation factor between ferric hydroxide [$Fe(OH)_3$] and aqueous Fe(II) ($\Delta^{56}Fe_{Fe(OH)_3-Fe(II)}$) varies between 4.0‰ and 2.6‰, depending on adsorption of Si to $Fe(OH)_3$ and incorporation of Si into $Fe(OH)_3$ (Wu et al., 2011, 2012). Ferric hydroxides (Si-free) produced by Fe(II)-oxidizing photoautotrophic bacteria are enriched in heavy Fe isotopes by ~1.5 ± 0.2‰ for $^{56}Fe/^{54}Fe$ ratios, likely reflecting an equilibrium $\Delta^{56}Fe_{Fe(OH)_3-Fe(II)}$ fractionation that is superimposed by a kinetic isotope effect upon precipitation that reduces the net Fe isotope fractionation (Croal et al., 2004). Experiments on Fe(II)-oxidizing, nitrate-reducing bacteria have produced apparent equilibrium $^{56}Fe/^{54}Fe$ fractionations between hydrous ferric oxide and $Fe(II)_{aq}$ of ~+3‰ (Kappler et al., 2010) in Si-free systems. If, however, Fe(II) oxidation is quantitative (complete), $Fe(OH)_3$ will inherit the Fe isotope composition of the initial aqueous Fe(II), producing an apparent $\Delta^{56}Fe_{Fe(OH)_3\text{-}Fe(II)}$ fractionation of zero (Pathway 1 in Fig. 5; Johnson et al., 2004). Therefore, the apparent Fe isotope fractionation between the precursors of hematite and aqueous Fe(II) could cover the range of 0–4‰, depending largely on the extent of oxidation, where the highest values would be produced by the smallest extent of oxidation.

Partial oxidation of hydrothermally sourced $Fe(II)_{aq}$ is one possible explanation of the positive $\delta^{56}Fe$ values for hematite in the Dales Gorge BIF (Pathway 2 in Fig. 5). Positive $\delta^{56}Fe$ values of ~+1 to +2‰ could be produced by 67–33% Fe(II) oxidation in a closed-system equilibrium model, or 83–52% Fe(II) oxidation in a Rayleigh model, assuming a $\Delta^{56}Fe_{Fe(OH)_3-Fe(II)}$ fractionation factor of +3‰. A more realistic approach to modeling $Fe(II)_{aq}$ oxidation in the photic zone is through a reaction-transport model (Czaja et al., 2012, 2013), and such a model requires smaller extents of oxidation to produce comparably high $\delta^{56}Fe$ values relative to a closed-system or Rayleigh model. Because, however, the average $\delta^{56}Fe$ value of ~2.5 Ga BIFs lies near zero (this study; Johnson et al., 2008b; Planavsky et al., 2012), which implies a near-complete overall oxidation of hydrothermal $Fe(II)_{aq}$, Fe(III) hydroxides produced by partial oxidation that had positive $\delta^{56}Fe$ values would be expected to comprise a small portion of the Fe(III) hydroxides produced. Further confirmation of near complete overall oxidation of hydrothermally sourced $Fe(II)_{aq}$ comes from Fe isotope data of broadly coeval low-Fe, Ca–Mg carbonates, which have highly negative $\delta^{56}Fe$ values (as low as −3.7‰, commonly −1 ~ −2‰; Czaja et al., 2012; von Blanckenburg et al., 2008). Essentially complete $Fe(II)_{aq}$ oxidation is required to produce highly negative $\delta^{56}Fe$ values in the small residual pool of $Fe(II)_{aq}$ in the photic zone, which was subsequently incorporated into the shallow-water Ca–Mg carbonates (Czaja et al., 2012).

Production of hematite that has negative $\delta^{56}Fe$ values (Pathways 3 and 4 in Fig. 5) requires different processes than those described above. Hematite that has negative $\delta^{56}Fe$ values cannot be explained by oxidation of aqueous Fe(II) that had a $\delta^{56}Fe$ value of 0‰, because the $\Delta^{56}Fe_{Fe(OH)_3-Fe(II)}$ fractionation cannot be negative. The negative $\delta^{56}Fe$ values of hematite are best explained by quantitative oxidation of aqueous Fe(II) that was already depleted in heavy Fe isotopes relative to hydrothermal fluid

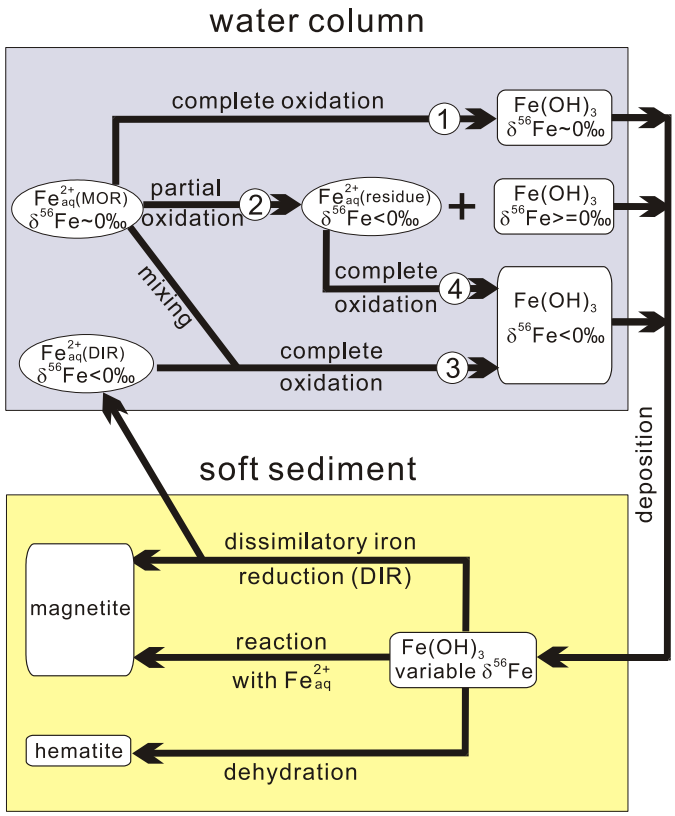

Fig. 5. Cartoon showing components and pathways for Fe isotope fractionations in genesis of magnetite and hematite in BIFs. Four possible pathways for producing the variable Fe isotope compositions of $Fe(OH)_3$ (precursors for hematite and magnetite) are labeled with numbers, and they are discussed in detail in Section 5.3 in the text.

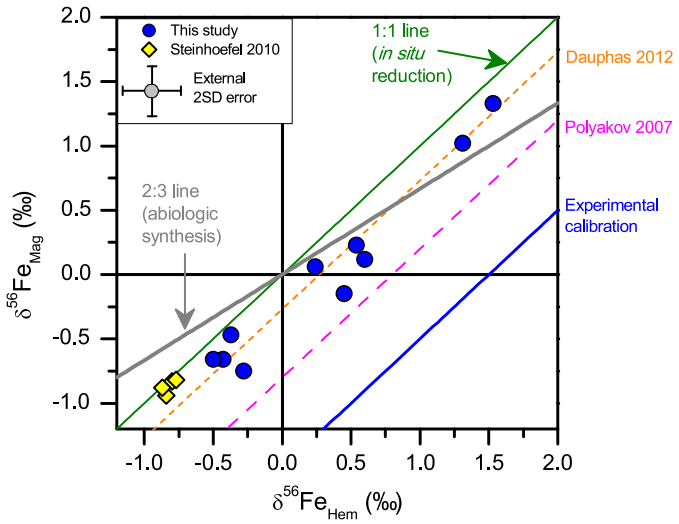

Fig. 6. Plot of Fe isotope compositions of coexisting hematite and magnetite in BIFs, together with trends that represent different pathways of magnetite formation, and equilibrium Fe isotope fractionation factors between hematite and magnetite, as predicted by theoretical calculation (Dauphas et al., 2012; Polyakov et al., 2007), and inferred from published laboratory experiments (see Section 5.3).

sources. Dissimilatory iron reduction (DIR) is a major pathway of iron recycling in soft sediments, where microbes use organic carbon as an electron donor to reduce Fe(III), releasing high concentrations of aqueous Fe(II) (Appendix 4) that has δ^{56}Fe values as much as 3‰ lower than the initial Fe(III) hydroxides (Bergquist and Boyle, 2006; Crosby et al., 2005, 2007; Homoky et al., 2009; Severmann et al., 2006, 2008; Staubwasser et al., 2006; Wu et al., 2009). Release of low-δ^{56}Fe aqueous Fe(II) that is recycled from Fe oxides from DIR back to the ocean, therefore, is one explanation for production of a low-δ^{56}Fe aqueous Fe(II) component in an Archean ocean (Pathway 3 in Fig. 5; Johnson et al., 2008a, 2008b). An alternative explanation for hematite that has negative δ^{56}Fe values is precipitation from seawater that had previously undergone extensive oxidation, producing very low δ^{56}Fe values in the remaining aqueous Fe(II) (Pathway 4 in Fig. 5; Anbar and Rouxel, 2007; Rouxel et al., 2005; Tsikos et al., 2010). Difficulty with the latter model in producing negative δ^{56}Fe values for Fe-rich rocks and minerals lies in the fact that extensive oxidation produces a Fe-poor low-δ^{56}Fe reservoir in a closed system, opposite of what is required to produce a low-δ^{56}Fe and Fe-rich pool.

Formation of magnetite in BIFs is commonly ascribed to reaction of poorly crystalline $Fe(OH)_3$ with an aqueous Fe(II) component from either hydrothermal activity (e.g., Klein, 2005) or that produced by DIR (Fig. 5; Johnson et al., 2008a; Walker, 1984), the latter reflecting the fact that magnetite is a common end product of microbial reduction of $Fe(OH)_3$ (Lovley et al., 1987). Because the δ^{56}Fe values of hematite and magnetite broadly overlap in the Dales Gorge BIF samples studied here (Fig. 6), although on average magnetite has a slightly lower δ^{56}Fe value, we focus here on the possible paragenetic relations between these minerals. Among the fifteen BIF samples analyzed in this study, six contain both hematite and magnetite, and the δ^{56}Fe values of magnetite from these six samples cover a range of −0.80 to +1.33‰, significantly greater than the range in δ^{56}Fe values for magnetite in the other 10 samples, which is −0.73 to +0.44‰. Notably, there is a linear relation between the δ^{56}Fe values of magnetite and those of co-existing hematite (Fig. 6). On a $\delta^{56}Fe_{Hem}$–$\delta^{56}Fe_{Mag}$ diagram, the data plot along a trend of $\delta^{56}Fe_{Mag} = \delta^{56}Fe_{Hem} - 0.29$ ($R^2 = 0.95$, Fig. 6), reflecting the slightly lower average δ^{56}Fe value for magnetite. Results of a previous *in situ* Fe isotope study on samples from BIF band 16 by Steinhoefel et al. (2010) also plot along this trend. As shown in Fig. 6, the majority of the data plot parallel a1:1 line, noted as "*in situ* reduction", where magnetite inherits the Fe isotope composition of $Fe(OH)_3$ precursors, but slightly offset toward the lines of "hematite–magnetite equilibrium" defined by theoretical predictions and laboratory experiments. Iron isotope fractionation between these two minerals ($\Delta^{56}Fe_{Hem\text{-}Mag}$) is calculated to be +0.8‰ at 25 °C by Polyakov et al. (2007) and +0.3‰ at 27 °C by Dauphas et al. (2012), respectively, whereas experimental studies on Fe isotope fractionation for the magnetite–$Fe(II)_{aq}$ pair (Frierdich et al., 2013; Johnson et al., 2005) and the hematite–$Fe(III)_{aq}$–$Fe(II)_{aq}$ pairs (Skulan et al., 2002; Welch et al., 2003; Wu et al., 2009, 2010) suggest a $\Delta^{56}Fe_{Hem\text{-}Mag}$ fractionation of ~+1.5‰; because the accuracy of calculated Fe isotope fractionation factors is difficult to assess, and can be highly dependent upon calculation method (see discussion in Polyakov and Soultanov, 2011), we will use the experimentally derived $\Delta^{56}Fe_{Hem\text{-}Mag}$ of +1.5‰ in the discussion below.

Precipitation of magnetite and hematite in equilibrium with seawater can be ruled out, because, as discussed above, the wide range of δ^{56}Fe and δ^{18}O values of the oxides strongly argues against a seawater origin. In addition, Fe isotope exchange between magnetite and hematite during diagenesis or low-grade burial metamorphism is an unlikely explanation for the $\delta^{56}Fe_{mag}$–$\delta^{56}Fe_{hem}$ relations in Fig. 6, given the very slow diffusion of Fe in hematite (Section 5.1). Production of magnetite through reaction of hydrothermally sourced $Fe(II)_{aq}$ (δ^{56}Fe~0‰) with hematite or $Fe(OH)_3$ of variable δ^{56}Fe values is also unlikely, because such a relation should plot along a line with a slope of 2/3 on Fig. 6, as 1/3 of Fe in magnetite would be of hydrothermal origin (δ^{56}Fe = 0‰). Moreover, reaction with hydrothermal $Fe(II)_{aq}$ should produce a mixing relation that passes through δ^{56}Fe = 0 for magnetite.

We suggest that the most likely scenario to explain the magnetite–hematite relations is that magnetite was formed in the soft sediment, where magnetite either inherited the Fe isotope composition of $Fe(OH)_3$ by *in situ* microbial reduction (Lovley et al., 1987), or underwent isotopic exchange with $Fe(II)_{aq}$ that was produced by DIR. Although measured organic carbon contents are very low in oxide-rich BIF samples (e.g., Klein, 2005; Klein and Beukes, 1989), and this has been used to argue against a role for biology in BIF genesis (Klein, 2005; Planavsky et al., 2012), the low δ^{13}C values of siderite in BIFs indicate that a significant amount of organic carbon existed in the soft sediments in the early stages of BIF formation (e.g., Craddock and Dauphas, 2011; Heimann et al., 2010). The high abundance of Fe(II) minerals in BIFs, if converted to the equivalent abundance of organic C, suggests initial organic C contents approaching 5 wt.% (Appendix 4), which is two to three orders-of-magnitudes higher than measured values. Such calculations demonstrate that initial deposition of BIFs was likely associated with significant reducing potential such that *in situ* conversion of $Fe(OH)_3$/hematite to low-Si magnetite could have occurred. Laboratory experiments of magnetite formation through DIR demonstrate that isotopic exchange between magnetite and $Fe(II)_{aq}$ may be rapid, and that on a mass-balance basis, the bulk δ^{56}Fe value of magnetite is largely inherited from the precursor Fe(III) oxide/hydroxides (Johnson et al., 2005). The fact that the hematite–magnetite pairs all plot slightly below the 1:1 line in Fig. 6 implies some degree of Fe isotope exchange between magnetite and the $Fe(OH)_3$ precursor, which shifted the system, to a small extent, towards isotope equilibrium (Fig. 6).

5.4. A model for Fe oxide formation in the Dales Gorge BIF based on combined O and Fe isotope variations

Co-variation in O and Fe isotopes for iron oxides from the Dales Gorge BIF (e.g., Fig. 4) demonstrates that these isotopic systems re-

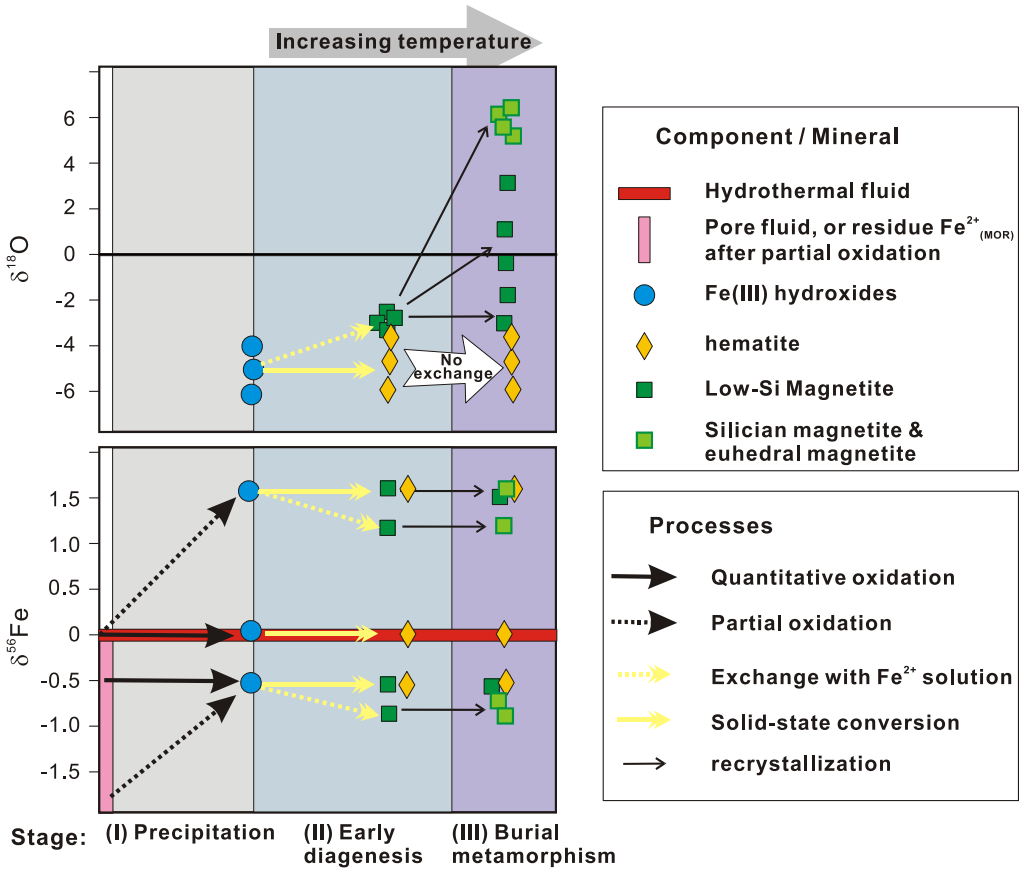

Fig. 7. A schematic diagram for genesis of magnetite and hematite in the Dales Gorge member BIF formation at Wittenoom, Hamersley Basin, Western Australia. It should be noted that the diagram shows generalized, inferred values of O and Fe isotope compositions for the minerals, and these are not actual measured values in this study, although they are representative of the results obtained. For detailed explanation, see Section 5.4.

spond to different aspects of the processes involved in BIF genesis, from initial precipitation in the photic zone to post-depositional diagenesis and metamorphism (Fig. 7).

In the initial stage of precipitation, hydrous $Fe(OH)_3$ formed via oxidation of aqueous Fe(II) either by free O_2 released by oxygenic photosynthetic bacteria, or by anoxygenic Fe-oxidizing photosynthetic bacteria (Czaja et al., 2013; Kappler et al., 2005). $\delta^{56}Fe$ values of aqueous Fe(II) varied between 0‰ and −0.6‰ or lower, depending on the relative contributions of hydrothermal Fe(II) and Fe(II) recycled by DIR, or the degree of Fe(II) oxidation in the ocean (Fig. 7). $Fe(OH)_3$ with $\delta^{56}Fe$ values close to 0‰ was produced by near-complete oxidation of aqueous Fe(II), and high $\delta^{56}Fe$ values were likely caused by partial oxidation of aqueous Fe(II). As products of bacterial photosynthesis, organic carbon was also deposited in the Hamersley Basin, together with $Fe(OH)_3$ and amorphous silica, and, likely Fe–Si co-precipitates. The O isotope composition of seawater is difficult to constrain, because of overprinting of O isotope compositions during conversion of $Fe(OH)_3$ to hematite and magnetite that occurred in the soft sediments.

During the second stage, which involved early diagenesis prior to lithification (Fig. 7), production of low-Si magnetite occurred through conversion of earlier Fe(III) oxide/hydroxides, where Fe(II) was most likely to have been generated by DIR, sustained by the high $Fe(OH)_3$ and organic carbon flux from the photic zone. If DIR did not generate large quantities of free $Fe(II)_{aq}$, or if significant $Fe(II)_{aq}$ was generated but mostly consumed via production of low-Si magnetite, the $\delta^{56}Fe$ values of solid-phase Fe during conversion would remain relatively constant based on mass-balance constraints. This would be accompanied, however, in the case of increasing temperatures during diagenesis, through increases in $\delta^{18}O$ values (Figs. 4, 7). Hematite likely has preserved early the O isotope compositions once conversion from $Fe(OH)_3$ to hematite occurred, due to extremely slow O isotope diffusion rates in hematite.

In the third stage, which involved burial metamorphism (Fig. 7), hydrothermal recrystallization of magnetite in the presence of silica-saturated fluids would produce the highest $\delta^{18}O$ values, as measured in the silician magnetite and euhedral magnetite. Dissolved Fe contents in the hydrous fluid phase, however, would likely remain quite low, because solubility of magnetite is low in the absence of high chloride or high temperature (>500 °C) conditions (Chou and Eugster, 1977; Holser and Schneer, 1961; Simon et al., 2004). Burial metamorphism at <350 °C would increase $\delta^{18}O$ values of magnetite but $\delta^{56}Fe$ values would remain little changed (Figs. 7), due to the lack of significant dissolved Fe in the fluids. Similarly, the euhedral magnetite, which reflects extensive recrystallization, would likely retain the $\delta^{56}Fe$ values of the early Fe(III) oxide/hydroxide precipitates, but would undergo an increase in $\delta^{18}O$ values through O isotope exchange at increased temperatures in the presence of a fluid (Fig. 7).

Overall, this model explains the lack of a correlation between Fe and O isotope compositions in Fe oxides in the Dales Gorge Member BIF. Iron isotopes record earlier processes including precipitation and early diagenesis, whereas O isotopes record later processes including diagenesis and burial metamorphism due to greater sensitivity to fluid interaction. The paragenesis of magnetite is clearly later than the initial $Fe(OH)_3$ precipitates or hematite produced by dehydration of $Fe(OH)_3$, and this is supported by the elevated $\delta^{18}O$ values for magnetite and petrographic relations. The 1:1 correlation between $\delta^{56}Fe$ values for magnetite

and hematite cannot be produced through equilibrium isotopic exchange, but instead suggests magnetite formation through *in situ* reduction of Fe(III) oxides/hydroxides via DIR.

6. Summary and conclusions

Combined *in situ* O and Fe isotope analyses of magnetite and hematite of the 2.45–2.50 Ga Dales Gorge Member BIF at Wittenoom of Hamersley Basin, Western Australia, document large variations in both O and Fe isotope compositions in the Fe oxides. Hematite has consistently low $\delta^{18}O$ values that range from $-8.8‰$ to $-0.6‰$. Three subgroups of magnetite, identified based on texture, composition, and BSE images, have different O isotope compositions. Euhedral magnetite and silician magnetite have high $\delta^{18}O$ values, ranging from 2.7‰ to 7.0‰, and 1.3 to 4.6‰, respectively, whereas low-Si magnetite cores of magnetite grains, or layers, have lower $\delta^{18}O$ values, ranging from -5.6 to 3.8‰. Large O isotope zoning between silician magnetite overgrowths and low-Si cores exists at μm-scales within single magnetite grains or layers. The variable $\delta^{18}O$ values of magnetite grains reflect variable degrees of isotopic exchange with fluids and variable temperatures up to ~300 °C during post-depositional processes.

In contrast to the common occurrence of fine-scale O isotope zonation, *in situ* analyses show Fe isotope homogeneity to ±0.2‰ for $^{56}Fe/^{54}Fe$ ratio in magnetite at sub-cm scales for the Dales Gorge member BIF samples, regardless of the difference in textures and O isotope variations among subgroups of magnetite. Although such homogeneity might be explained by fast diffusion of Fe in magnetite at <300 °C during metamorphism, there is a >2‰ variation in $\delta^{56}Fe$ values between the Dales Gorge member BIF samples, indicating isotope heterogeneity at scales greater than centimeters. The large variation in $\delta^{56}Fe$ values of iron oxides is interpreted to reflect Fe isotope variability of Fe(III) hydroxide precipitates produced through variable extents of oxidation and oxidation/precipitation from aqueous Fe(II) of variable isotopic compositions depending on the proportion of hydrothermal and microbial Fe(III) reduction sources. In samples that have coexisting hematite and magnetite, the $\delta^{56}Fe$ values of magnetite follow those of hematite but are consistently lower by 0.3‰ on average, over a $\delta^{56}Fe$ range of -0.56 to $+1.53‰$ for hematite. This relation implies that magnetite to a large extent inherited the Fe isotope compositions of the $Fe(OH)_3$ precursors, as may occur during microbial Fe(III) reduction when $Fe(II)_{aq}$ contents are low, but small extents of isotopic exchange during and after magnetite formation has slightly shifted the magnetite–hematite pairs towards isotope equilibrium.

Combined *in situ* O and Fe isotope analyses highlight the contrasting behavior of the O and Fe isotopes in hematite and magnetite in BIFs. Oxygen isotope variations in iron oxides of BIFs are mainly controlled by processes during and after early diagenesis (Fig. 7), and we can use *in situ* O isotope analysis to study post-depositional fluid–mineral interactions on BIFs. In contrast, Fe isotope variations in iron oxides of BIFs are mainly controlled by processes that occurred prior to burial metamorphism (Fig. 7), and *in situ* Fe isotope analysis provides insight into Fe pathways in the photic zone and the soft sediments during early diagenesis, prior to significant burial metamorphism. Therefore, *in situ* O and Fe isotope analyses are a powerful combination that provides a deeper understanding of BIF genesis than that of the individual isotopic systems by themselves, providing new constraints on the use of BIFs as proxies for paleo-environmental conditions and microbial processes.

Acknowledgements

Phil Gopon and Zhizhang Shen assisted in SEM analyses. We thank two anonymous reviewers for constructive reviews of the manuscript, and Prof. T. Mark Harrison for editorial handling and comments. WiscSIMS is partially supported by NSF-EAR (1053466). This study was supported by the NASA Astrobiology Institute.

Appendix A. Supplementary material

Supplementary material related to this article can be found online at http://dx.doi.org/10.1016/j.epsl.2013.10.014.

References

Amami, B., Addou, M., Millot, F., Sabioni, A., Monty, C., 1999. Self-diffusion in α-Fe_2O_3 natural single crystals. Ionics 5, 358–370.
Anbar, A.D., Rouxel, O., 2007. Metal stable isotopes in paleoceanography. Annu. Rev. Earth Planet. Sci. 35, 717–746.
Bao, H., Koch, P.L., 1999. Oxygen isotope fractionation in ferric oxide-water systems: low temperature synthesis. Geochim. Cosmochim. Acta 63, 599–613.
Baur, M.E., Hayes, J.M., Studley, S.A., Walter, M.R., 1985. Millimeter-scale variations of stable isotope abundances in carbonates from banded iron-formations in the Hamersley Group of Western Australia. Econ. Geol. 80, 270–282.
Beard, B.L., Johnson, C.M., Skulan, J.L., Nealson, K.H., Cox, L., Sun, H., 2003. Application of Fe isotopes to tracing the geochemical and biological cycling of Fe. Chem. Geol. 195, 87–117.
Becker, R.H., Clayton, R.N., 1972. Carbon isotopic evidence for the origin of a banded iron-formation in Western Australia. Geochim. Cosmochim. Acta 36, 577–595.
Becker, R.H., Clayton, R.N., 1976. Oxygen isotope study of a Precambrian banded iron-formation, Hamersley Range, Western Australia. Geochim. Cosmochim. Acta 40, 1153–1165.
Bekker, A., Slack, J.F., Planavsky, N., Krapež, B., Hofmann, A., Konhauser, K.O., Rouxel, O.J., 2010. Iron formation: the sedimentary product of a complex interplay among mantle, tectonic, oceanic and biospheric processes. Econ. Geol. 105, 467–508.
Bergquist, B.A., Boyle, E.A., 2006. Iron isotopes in the Amazon River system: Weathering and transport signatures. Earth Planet. Sci. Lett. 248, 54–68.
Chang, R.H., Wagner, J.B., 1972. Direct-current conductivity and iron tracer diffusion in hematite at high temperatures. J. Am. Ceram. Soc. 55, 211–213.
Chou, I.M., Eugster, H.P., 1977. Solubility of magnetite in supercritical chloride solutions. Am. J. Sci. 277, 1296–1314.
Clayton, R.N., Kieffer, S.W., 1991. Oxygen isotopic thermometer calibrations. In: Taylor, H.P., O'Neil, J.R., Kaplan, I.R. (Eds.), Stable Isotope Geochemistry. Geochemical Society, pp. 365–413.
Craddock, P.R., Dauphas, N., 2011. Iron and carbon isotope evidence for microbial iron respiration throughout the Archean. Earth Planet. Sci. Lett. 303, 121–132.
Crank, J., 1975. The Mathematics of Diffusion. Oxford University Press, Oxford.
Croal, L.R., Johnson, C.M., Beard, B.L., Newman, D.K., 2004. Iron isotope fractionation by Fe(II)-oxidizing photoautotrophic bacteria. Geochim. Cosmochim. Acta 68, 1227–1242.
Crosby, H.A., Johnson, C.M., Roden, E.E., Beard, B.L., 2005. Coupled Fe(II)–Fe(III) electron and atom exchange as a mechanism for Fe isotope fractionation during dissimilatory iron oxide reduction. Environ. Sci. Technol. 39, 6698–6704.
Crosby, H.A., Roden, E.E., Johnson, C.M., Beard, B.L., 2007. The mechanisms of iron isotope fractionation produced during dissimilatory Fe(III) reduction by Shewanella putrefaciens and Geobacter sulfurreducens. Geobiology 5, 169–189.
Czaja, A.D., Johnson, C.M., Beard, B.L., Roden, E.E., Li, W., Moorbath, S., 2013. Biological Fe oxidation controlled deposition of banded iron formation in the ca. 3770 Ma Isua Supracrustal Belt (West Greenland). Earth Planet. Sci. Lett. 363, 192–203.
Czaja, A.D., Johnson, C.M., Roden, E.E., Beard, B.L., Voegelin, A.R., Nagler, T.F., Beukes, N.J., Wille, M., 2012. Evidence for free oxygen in the Neoarchean ocean based on coupled iron-molybdenum isotope fractionation. Geochim. Cosmochim. Acta 86, 118–137.
Dauphas, N., Roskosz, M., Alp, E.E., Golden, D.C., Sio, C.K., Tissot, F.L.H., Hu, M.Y., Zhao, J., Gao, L., Morris, R.V., 2012. A general moment NRIXS approach to the determination of equilibrium Fe isotopic fractionation factors: Application to goethite and jarosite. Geochim. Cosmochim. Acta 94, 254–275.
Ewers, W.E., Morris, R.C., 1981. Studies of the Dales Gorge Member of the Brockman Iron Formation, Western Australia. Econ. Geol. 76, 1929–1953.
Frierdich, A.J., Beard, B.L., Scherer, M.M., Johnson, C.M., 2013. Iron isotope exchange and fractionation between aqueous Fe(II) and magnetite: implications for equilibrium iron isotope fractionation factors and interpreting iron isotope compositions in the rock record. In: GSA 125th Anniversary Annual Meeting Abstract. The Geological Society of America, Denver, Colorado.
Giletti, B.J., Hess, K.C., 1988. Oxygen diffusion in magnetite. Earth Planet. Sci. Lett. 89, 115–122.

Gregory, R.T., Criss, R.E., 1986. Isotopic exchange in open and closed systems. Rev. Mineral. Geochem. 16, 91–127.

Hallstrom, S., Hoglund, L., Agren, J., 2011. Modeling of iron diffusion in the iron oxides magnetite and hematite with variable stoichiometry. Acta Mater. 59, 53–60.

Heck, P.R., Huberty, J.M., Kita, N.T., Ushikubo, T., Kozdon, R., Valley, J.W., 2011. SIMS analyses of silicon and oxygen isotope ratios for quartz from Archean and Paleoproterozoic banded iron formations. Geochim. Cosmochim. Acta 75, 5879–5891.

Heimann, A., Johnson, C.M., Beard, B.L., Valley, J.W., Roden, E.E., Spicuzza, M.J., Beukes, N.J., 2010. Fe, C, and O isotope compositions of banded iron formation carbonates demonstrate a major role for dissimilatory iron reduction in ~2.5 Ga marine environments. Earth Planet. Sci. Lett. 294, 8–18.

Holland, H.D., 1984. The Chemical Evolution of the Atmosphere and Oceans. Princeton University Press.

Holser, W.T., Schneer, C.J., 1961. Hydrothermal magnetite. Geol. Soc. Am. Bull. 72, 369–385.

Homoky, W.B., Severmann, S., Mills, R.A., Statham, P.J., Fones, G.R., 2009. Pore-fluid Fe isotopes reflect the extent of benthic Fe redox recycling: Evidence from continental shelf and deep-sea sediments. Geology 37, 751–754.

Horn, I., von Blanckenburg, F., Schoenberg, R., Steinhoefel, G., Markl, G., 2006. In situ iron isotope ratio determination using UV-femtosecond laser ablation with application to hydrothermal ore formation processes. Geochim. Cosmochim. Acta 70, 3677–3688.

Huberty, J.M., Kita, N.T., Heck, P.R., Kozdon, R., Fournelle, J.H., Xu, H., Valley, J.W., 2010a. In situ $\delta^{18}O$ analyses in quartz and magnetite from the Dale Gorge BIF. In: 5th International Archean Symposium. Perth, Australia.

Huberty, J.M., Kita, N.T., Kozdon, R., Heck, P.R., Fournelle, J.H., Spicuzza, M.J., Xu, H., Valley, J.W., 2010b. Crystal orientation effects in $\delta^{18}O$ for magnetite and hematite by SIMS. Chem. Geol. 276, 269–283.

Huberty, J.M., Konishi, H., Heck, P.R., Fournelle, J.H., Valley, J.W., Xu, H., 2012. Silician magnetite from the Dales Gorge Member of the Brockman Iron Formation, Hamersley Group, Western Australia. Am. Mineral. 97, 26–37.

Hyslop, E., Valley, J., Johnson, C., Beard, B., 2008. The effects of metamorphism on O and Fe isotope compositions in the Biwabik Iron Formation northern Minnesota. Contrib. Mineral. Petrol. 155, 313–328.

James, H.L., 1954. Sedimentary facies of iron-formation. Econ. Geol. 49, 235–293.

Johnson, C.M., Beard, B.L., Albarede, F., 2004. Overview and general concepts. In: Johnson, C.M., Beard, B.L., Albarede, F. (Eds.), Geochemistry of Non-traditional Stable Isotopes. The Mineralogical Society of America, Washington, DC, pp. 1–22.

Johnson, C.M., Beard, B.L., Beukes, N.J., Klein, C., O'Leary, J.M., 2003. Ancient geochemical cycling in the Earth as inferred from Fe isotope studies of banded iron formations from the Transvaal Craton. Contrib. Mineral. Petrol. 144, 523–547.

Johnson, C.M., Beard, B.L., Klein, C., Beukes, N.J., Roden, E.E., 2008a. Iron isotopes constrain biologic and abiologic processes in banded iron formation genesis. Geochim. Cosmochim. Acta 72, 151–169.

Johnson, C.M., Beard, B.L., Roden, E.E., 2008b. The Iron isotope fingerprints of redox and biogeochemical cycling in modern and ancient Earth. Annu. Rev. Earth Planet. Sci. 36, 457–493.

Johnson, C.M., Ludois, J.M., Beard, B.L., Beukes, N.J., Heimann, A., in press. Iron formation carbonates: Paleoceanographic proxy or recorder of microbial diagenesis? Geology, http://dx.doi.org/10.1130/G34698.1.

Johnson, C.M., Roden, E.E., Welch, S.A., Beard, B.L., 2005. Experimental constraints on Fe isotope fractionation during magnetite and Fe carbonate formation coupled to dissimilatory hydrous ferric oxide reduction. Geochim. Cosmochim. Acta 69, 963–993.

Kappler, A., Johnson, C.M., Crosby, H.A., Beard, B.L., Newman, D.K., 2010. Evidence for equilibrium iron isotope fractionation by nitrate-reducing iron(II)-oxidizing bacteria. Geochim. Cosmochim. Acta 74, 2826–2842.

Kappler, A., Pasquero, C., Konhauser, K.O., Newman, D.K., 2005. Deposition of banded iron formations by anoxygenic phototrophic Fe(II)-oxidizing bacteria. Geology 33, 865–868.

Kaufman, A.J., 1996. Geochemical and mineralogic effects of contact metamorphism on banded iron-formation: an example from the Transvaal Basin, South Africa. Precambrian Res. 79, 171–194.

Kaufman, A.J., Hayes, J.M., Klein, C., 1990. Primary and diagenetic controls of isotopic compositions of iron-formation carbonates. Geochim. Cosmochim. Acta 54, 3461–3473.

Kelly, J.L., Fu, B., Kita, N.T., Valley, J.W., 2007. Optically continuous silcrete quartz cements of the St. Peter Sandstone: High precision oxygen isotope analysis by ion microprobe. Geochim. Cosmochim. Acta 71, 3812–3832.

Kingery, W.D., Hill, D.C., Nelson, R.P., 1960. Oxygen Mobility in Polycrystalline $NiCr_2O_4$ and α-Fe_2O_3. J. Am. Ceram. Soc. 43, 473–475.

Kita, N.T., Huberty, J.M., Kozdon, R., Beard, B.L., Valley, J.W., 2011. High-precision SIMS oxygen, sulfur and iron stable isotope analyses of geological materials: accuracy, surface topography and crystal orientation. Surf. Interface Anal. 43, 427–431.

Kita, N.T., Ushikubo, T., Fu, B., Valley, J.W., 2009. High precision SIMS oxygen isotope analysis and the effect of sample topography. Chem. Geol. 264, 43–57.

Klein, C., 2005. Some Precambrian banded iron-formations (BIFs) from around the world: Their age, geologic setting, mineralogy, metamorphism, geochemistry and origins. Am. Mineral. 90, 1473–1499.

Klein, C., Beukes, N.J., 1989. Geochemistry and sedimentology of a facies transition from limstone to iron-formation deposition in the early Proterozoic Transvaal Supergroup, South Africa. Econ. Geol. 84, 1733–1774.

Lovley, D.R., Stolz, J.F., Nord, G.L., Phillips, E.J.P., 1987. Anaerobic production of magnetite by a dissimilatory iron-reducing microorganism. Nature 330, 252–254.

Marin-Carbonne, J., Rollion-Bard, C., Luais, B., 2011. In-situ measurements of iron isotopes by SIMS: MC-ICP-MS intercalibration and application to a magnetite crystal from the Gunflint chert. Chem. Geol. 285, 50–61.

Perry, E.C., Tan, F.C., Morey, G.B., 1973. Geology and stable isotope geochemistry of the Biwabik Iron Formation, Northern Minnesota. Econ. Geol. 68, 1110–1125.

Planavsky, N., Rouxel, O.J., Bekker, A., Hofmann, A., Little, C.T.S., Lyons, T.W., 2012. Iron isotope composition of some Archean and Proterozoic iron formations. Geochim. Cosmochim. Acta 80, 158–169.

Polyakov, V.B., Clayton, R.N., Horita, J., Mineev, S.D., 2007. Equilibrium iron isotope fractionation factors of minerals: Reevaluation from the data of nuclear inelastic resonant X-ray scattering and Mossbauer spectroscopy. Geochim. Cosmochim. Acta 71, 3833–3846.

Polyakov, V.B., Soultanov, D.M., 2011. New data on equilibrium iron isotope fractionation among sulfides: Constraints on mechanisms of sulfide formation in hydrothermal and igneous systems. Geochim. Cosmochim. Acta 75, 1957–1974.

Rasmussen, B., Fletcher, I.R., Sheppard, S., 2005. Isotopic dating of the migration of a low-grade metamorphic front during orogenesis. Geology 33, 773–776.

Rouxel, I.J., Bekker, N., Edwards, A.J., 2005. Iron isotope constraints on the Archean and Paleoproterozoic ocean redox state. Science 307, 1088–1091.

Severmann, S., Johnson, C.M., Beard, B.L., McManus, J., 2006. The effect of early diagenesis on the Fe isotope compositions of porewaters and authigenic minerals in continental margin sediments. Geochim. Cosmochim. Acta 70, 2006–2022.

Severmann, S., Lyons, T.W., Anbar, A., McManus, J., Gordon, G., 2008. Modern iron isotope perspective on the benthic iron shuttle and the redox evolution of ancient oceans. Geology 36, 487–490.

Simon, A.C., Pettke, T., Candela, P.A., Piccoli, P.M., Heinrich, C.A., 2004. Magnetite solubility and iron transport in magmatic-hydrothermal environments. Geochim. Cosmochim. Acta 68, 4905–4914.

Skulan, J.L., Beard, B.L., Johnson, C.M., 2002. Kinetic and equilibrium Fe isotope fractionation between aqueous Fe(III) and hematite. Geochim. Cosmochim. Acta 66, 2995–3015.

Staubwasser, M., von Blanckenburg, F., Schoenberg, R., 2006. Iron isotopes in the early marine diagenetic iron cycle. Geology 34, 629–632.

Steinhoefel, G., Horn, I., von Blanckenburg, F., 2009. Micro-scale tracing of Fe and Si isotope signatures in banded iron formation using femtosecond laser ablation. Geochim. Cosmochim. Acta 73, 5343–5360.

Steinhoefel, G., von Blanckenburg, F., Horn, I., Konhauser, K.O., Beukes, N.J., Gutzmer, J., 2010. Deciphering formation processes of banded iron formations from the Transvaal and the Hamersley successions by combined Si and Fe isotope analysis using UV femtosecond laser ablation. Geochim. Cosmochim. Acta 74, 2677–2696.

Trendall, A.F., Blockley, J.G., 1968. Stratigraphy of the Dales Gorge Member of the Brockman Iron formation in the Precambrian Hamersley Group of Western Australia. In: Geological Survey of Western Australia Annual Report for 1967, pp. 48–53.

Trendall, A.F., Blockley, J.G., 1970. The iron-formations of the Precambrian Hamersley Group, Western Australia. Geol. Surv. West. Aust. Bull. 119.

Trendall, A.F., Compston, W., Nelson, D.R., De Laeter, J.R., Bennett, V.C., 2004. SHRIMP zircon ages constraining the depositional chronology of the Hamersley Group, Western Australia. Aust. J. Earth Sci. 51, 621–644.

Trendall, A.F., Morris, R.C., 1983. Iron-Formation: Facts and Problems. Elsevier, Amsterdam.

Tsikos, H., Matthews, A., Erel, Y., Moore, J.M., 2010. Iron isotopes constrain biogeochemical redox cycling of iron and manganese in a Palaeoproterozoic stratified basin. Earth Planet. Sci. Lett. 298, 125–134.

Valley, J.W., 2001. Stable isotope thermometry at high temperatures. Rev. Mineral. Geochem. 43, 365–413.

von Blanckenburg, F., Mamberti, M., Schoenberg, R., Kamber, B.S., Webb, G.E., 2008. The iron isotope composition of microbial carbonate. Chem. Geol. 249, 113–128.

Walker, J.C.G., 1984. Suboxic diagenesis in banded iron formations. Nature 309, 340–342.

Watson, E.B., Cherniak, D.J., Frank, E.A., 2009. Retention of biosignatures and mass-independent fractionations in pyrite: Self-diffusion of sulfur. Geochim. Cosmochim. Acta 73, 4792–4802.

Welch, S.A., Beard, B.L., Johnson, C.M., Braterman, P.S., 2003. Kinetic and equilibrium Fe isotope fractionation between aqueous Fe(II) and Fe(III). Geochim. Cosmochim. Acta 67, 4231–4250.

Whitehouse, M.J., Fedo, C.M., 2007. Microscale heterogeneity of Fe isotopes in >3.71 Ga banded iron formation from the Isua Greenstone Belt, southwest Greenland. Geology 35, 719–722.

Williford, K.H., Van Kranendonk, M.J., Ushikubo, T., Kozdon, R., Valley, J.W., 2011. Constraining atmospheric oxygen and seawater sulfate concentrations during Paleoproterozoic glaciation: In situ sulfur three-isotope microanalysis of pyrite from the Turee Creek Group, Western Australia. Geochim. Cosmochim. Acta 75, 5686–5705.

Winter, B.L., Knauth, L.P., 1992. Stable isotope geochemistry of cherts and carbonates from the 2.0 Ga gunflint iron formation: implications for the depositional setting and the effects of diagenesis and metamorphism. Precambrian Res. 59, 283–313.

Wu, L., Beard, B.L., Roden, E.E., Johnson, C.M., 2009. Influence of pH and dissolved Si on Fe isotope fractionation during dissimilatory microbial reduction of hematite. Geochim. Cosmochim. Acta 73, 5584–5599.

Wu, L., Beard, B.L., Roden, E.E., Johnson, C.M., 2011. Stable iron isotope fractionation between aqueous Fe(II) and hydrous ferric oxide. Environ. Sci. Technol. 45, 1847–1852.

Wu, L., Beard, B.L., Roden, E.E., Kennedy, C.B., Johnson, C.M., 2010. Stable Fe isotope fractionations produced by aqueous Fe(II)–hematite surface interactions. Geochim. Cosmochim. Acta 74, 4249–4265.

Wu, L., Percak-Dennett, E.M., Beard, B.L., Roden, E.E., Johnson, C.M., 2012. Stable iron isotope fractionation between aqueous Fe(II) and model Archean ocean Fe–Si coprecipitates and implications for iron isotope variations in the ancient rock record. Geochim. Cosmochim. Acta 84, 14–28.

Yapp, C.J., 1990. Oxygen isotopes in iron (III) oxides: 1. Mineral-water fractionation factors. Chem. Geol. 85, 329–335.

Yoshiya, K., Nishizawa, M., Sawaki, Y., Ueno, Y., Komiya, T., Yamada, K., Yoshida, N., Hirata, T., Wada, H., Maruyama, S., 2012. In situ iron isotope analyses of pyrite and organic carbon isotope ratios in the Fortescue Group: Metabolic variations of a Late Archean ecosystem. Precambrian Res. 212–213, 169–193.

Zheng, Y.-F., 1991. Calculation of oxygen isotope fractionation in metal oxides. Geochim. Cosmochim. Acta 55, 2299–2307.